Continuum-based modeling large-strain plastic deformation of semi-crystalline polyethylene systems: Implication of texturing and amorphicity

Zhu Yan, Qiang Guo, Fahmi Zaïri, Ali Zaoui, Qifeng Jiang, Xiaobing Liu

Continuum-based modeling large-strain plastic deformation of semi-crystalline polyethylene systems: Implication of texturing and amorphicity

Zhu Yan[a,b], Qiang Guo[c], Fahmi Zaïri[a*], Ali Zaoui[a], Qifeng Jiang[b], Xiaobing Liu[b]

[a]Univ. Lille, IMT Lille Douai, Univ. Artois, JUNIA, ULR 4515 - LGCgE, Laboratoire de Génie Civil et géo-Environnement, F-59000 Lille, France
[b]Xihua University, Key Laboratory of Fluid and Power Machinery, 610039 Sichuan, China
[c]Department of Mechanical Engineering, University of Colorado Boulder, Boulder, 80309, USA

*Corresponding author.
E-mail address: fahmi.zairi@polytech-lille.fr

Abstract

The present contribution examines the ability of a constitutive model to capture polyethylene response variation with crystallinity. The model considers the elastic-viscoplastic crystal deformation and anisotropy due to the crystallographic texturing along with the amorphous chains network elastic-viscoplastic-viscohyperelastic deformation. The coupling between the two phases is performed by means of a multi-scale homogenization-based approach in which the interfacial interaction is considered. The model is applied on semi-crystalline polyethylene systems containing a broad range of crystallinities. Both monotonic and oligo-cyclic tensile loading sequences are considered upon large-strain plastic deformation. The model is found able to correctly capture the gradual transition of the rate-dependent monotonic response from a thermoplastic-like behavior at high crystallinity to a nearly elastomeric-like behavior at low crystallinity. The model abilities to capture cyclically loaded polyethylene systems are critically discussed. The influential and decisive role of the amorphous chains network alignment/relaxation on the cyclic stretching is emphasized by analyzing local stresses and stretches.

Keywords: Semi-crystalline polyethylene; Crystallographic texturing; Amorphicity; Oligo-cyclic loading; Viscoplastic-viscohyperelastic modeling.

1. Introduction

Semi-crystalline polyethylene systems have a large range of applications, in sectors like oil industry, automobile, aeronautic, robotic, biomechanics and civil engineering, in which they

may be subjected to large strains under in-service or manufacturing process. These materials present an extremely large variety of molecular architectures with a crystallinity index ranged from about seventy percent down to a few percent only, passing the morphology from well-organized crystalline lamellae to discrete crystalline lamellae randomly dispersed within an amorphous matrix (Peacock, 2000). The broad morphology range leads basically to an extremely large variety of responses from the plastic response characteristics of thermoplastics to the nonlinear elastic response characteristics of elastomers (Ayoub et al., 2011; Abdul-Hameed et al., 2014) with a profound influence of the amorphous and crystalline features such as density of stress transmitters in the amorphous layers and crystal dimensions (Hillmansen et al., 2000; Argon et al., 2005; Kazmierczak et al., 2005; Bartczak and Galeski, 2010). The development of continuum-based models is a prerequisite for designing and performance predicting polyethylene-based products whether in the form of fibers, films or massive parts.

Modeling response of semi-crystalline polyethylene systems is to relate to their complex organization hierarchy from the nano-sized lamellar structure to the macroscopic scale. Purely phenomenological approaches using theories such as viscoelasticity (Zhang and Moore, 1997) or viscoplasticity (Drozdov and Gupta, 2003; Colak and Dusunceli, 2006; Zaïri et al., 2006; Khan and Krempl, 2006; Ben Hadj Hamouda et al., 2007; Dusunceli and Colak, 2008; Drozdov et al., 2013) have the advantage of simplicity. Nonetheless, these models provide only a mathematical description of the different aspects of the material response, generally under low-strain and without obvious connection to the actual microstructure and its deformation-induced evolution. Over the years, continuum-based models have been developed with the concern to introduce microstructural specificities as precisely as possible in the aim to provide a deep understanding of the separate and synergic effects of key microstructural parameters governing the macroscopic response. The link with the microstructure strongly depends on the approach used for the constitutive representation and the observation scale from which the model starts. In the most physically consistent models, the microstructure approximation of semi-crystalline polymer systems is generally based on composite-type representations.

Following the pioneering work of Haward and Thackray (1968), continuum-based models have been proposed to constitutively describe the large-strain material behavior of semi-crystalline polymers by the combination of resistances representing intermolecular and molecular network micro-mechanisms (Ayoub et al., 2010, 2011; Abdul-Hameed et al., 2014; Makki et al., 2017; Sepiani et al., 2018; Chen et al., 2019; Deplancke et al., 2019; Qi et al., 2019; Bernard et al., 2020). The latter micro-mechanism describes the resistance to deformation of the amorphous molecular structure to simulate the molecular orientation/relaxation process during the strain-hardening stage of the stress-strain response (Boyce et al., 2000). In the above-cited models, a simple averaging homogenization is used and only for the intermolecular resistance which does not allow to represent the crystallinity effect on the deformation-induced orientation. The active interaction between crystalline and amorphous domains is a first-order factor which requires to be taken into account using more sophisticated micromechanics-based approaches. For instance, micromechanics-based models using the Eshelby inclusion theory were proposed through the matrix-inclusion constitutive representation of the semi-crystalline polymer system (Bédoui et al., 2006; Gueguen et al., 2010; Anoukou et al., 2014; Hachour et al., 2014). These models were restricted to the elastic stiffness and yield strength predictions, and more recently extended to the small-strain post-yielding behavior (Mesbah et al., 2021). Multi-scale homogenization-based constitutive models have been also developed by considering at the mesoscopic scale an aggregate of two-phase layered composite inclusions consisting in parallel crystalline lamellae and amorphous layers. Using this concept, the elastic-viscoplastic deformation behavior of high-density polyethylene was predicted at small strain levels (Nikolov and Doghri, 2000; Nikolov et al., 2002) and moderate strain levels by simulating the texture evolution (Lee et al., 1993a, 1993b; van Dommelen et al., 2003; Agoras and Ponte Castaneda, 2012; Uchida and Tada, 2013; Mirkhalaf et al., 2019). The models are generally identified using loading modes in which the crystal plasticity is a first-order phenomenon, such as compression, channel die compression and shear. While the local events involved in yielding due to tensile straining are not connected with clear crystal shearing but with the phenomena occurring in the amorphous phase and the relation to crystal thickness is not expected, rather to crystallinity degree, read amorphicity (Seguela et al., 1998a, 1998b;

Bartczak and Kozanecki, 2005; Bartczak and Galeski, 2010; Rozanski and Galeski, 2013). The latter is an influential and decisive parameter in tensile yielding, the strength and consistency of the amorphous phase being thus first-order factors (Mesbah et al., 2021).

The aim of the present article is to examine the ability of a multi-scale homogenization-based constitutive model to capture the polyethylene large-strain tensile response variation with crystal concentration. The model is applied on a high-density polyethylene with 0.72 crystal content, a low-density polyethylene with 0.3 crystal content and an ultra-low-density polyethylene with 0.15 crystal content. The results of our simulations are criticized by analyzing the model ability to capture a series of experimental observations under monotonic, loading-unloading and oligo-cyclic stretching over a large strain range. The effect of the amorphous phase fraction on the microstructure evolution is finally discussed thanks to the model.

The present paper is organized as follows. Section 2 presents the fully three-dimensional continuum-based constitutive theory. The model-experiments comparisons are presented and discussed in Section 3. Concluding remarks are finally given in Section 4.

The following notation is used throughout the text. Tensors and vectors are denoted by normal boldfaced letters and italicized boldfaced letters, respectively, while scalars and individual components of vectors and tensors are denoted by normal italicized letters. The superposed dot designates the time derivative. The superscript T indicates the transpose quantity.

2. Model presentation

2.1. Constitutive representation

The organization hierarchy of the semi-crystalline polyethylene structure depends on the amorphicity. As illustrated in Fig. 1, decreasing the crystallinity leads to a morphology transition from micro-sized interconnecting spherulites to individually crystalline lamellae randomly dispersed in the rubbery amorphous matrix. According to the microstructure approximation based on a composite-type description, the morphology may be regarded as a percolated crystalline matrix at high crystallinity and a rubbery matrix at low crystallinity. A constitutive representation unifying these views is illustrated in Fig. 2. At the mesoscopic scale, the representative volume element of the heterogeneous material is seen as a mixture of

crystalline and amorphous domains organized as an aggregate of two-phase layered composite inclusions which are randomly oriented, the macroscopic response being obtained by the averaging homogenization. The relative thickness of the two layers determines the crystal concentrations, which allows to consider high-to-low crystalline structures. Both crystalline lamella and amorphous layer are homogeneous and continuous media. The crystalline lamella consists of regularly ordered chains resulting in an orthorhombic structure with a high elastic modulus in the chain direction while the amorphous layer consists of randomly oriented entangled chains and is thus supposed to be an isotropic medium.

2.2. Constitutive equations

In what follows, the three-dimensional constitutive equations are described for the different physical sources governing the macro-response. The model satisfies the continuum mechanics rules within the large inelastic deformation kinematics. In the latter framework, the deformation gradient tensor $\mathbf{F}=\nabla \boldsymbol{x}\left(\boldsymbol{X},t\right)$ is introduced to map a material point from its initial position $\boldsymbol{X}$ in the reference configuration to its actual position x in the deformed configuration. The inelastic deformation mechanisms within each phase are considered to be distinct, and are described using the multiplicative decomposition concept of the deformation. The introduction of an intermediate configuration during a spontaneous elastic unloading allows the multiplicative deformation decomposition into elastic and inelastic parts: $\mathbf{F}=\mathbf{F}^{e}\mathbf{F}^{in}$ in which the elastic and inelastic components are depicted by superscripts *e* and *in*, respectively. The two tensors can be further decomposed into stretch (right $\mathbf{U}$ or left $\mathbf{V}$) and rotation $\mathbf{R}$ movements using the polar decomposition: $\mathbf{F}^{e}=\mathbf{R}^{e}\mathbf{U}^{e}=\mathbf{V}^{e}\mathbf{R}^{e}$ and $\mathbf{F}^{in}=\mathbf{R}^{in}\mathbf{U}^{in}=\mathbf{V}^{in}\mathbf{R}^{in}$. The subscripts *c* and *a* are used to differentiate the crystalline and amorphous phases, respectively.

2.2.1. Elastic-viscoplastic-viscohyperelastic polyethylene amorphous network

We assume that the behavior of the amorphous domain is the sum of an elastic-viscoplastic resistance that accounts for intermolecular interactions and a viscohyperelastic resistance that accounts for molecular network stretching and orientation process, the two physically distinct

sources acting in parallel. The amorphous Cauchy stress tensor $\boldsymbol{\sigma}_a$ is thus split into intermolecular stress $\boldsymbol{\sigma}_{a\_inter}$ and network stress $\boldsymbol{\sigma}_{a\_net}$:

$$\boldsymbol{\sigma}_a = \boldsymbol{\sigma}_{a\_inter} + \boldsymbol{\sigma}_{a\_net} \tag{1}$$

From the rheological point of view, the intermolecular resistance is represented by an elastic spring in series with a viscous dashpot (Fig. 2). The intermolecular Cauchy stress $\boldsymbol{\sigma}_{a\_inter}$ is constitutively coordinated with the corresponding strain by the following relationship:

$$\boldsymbol{\sigma}_{a\_\text{inter}} = \frac{1}{J_{a\_\text{inter}}} \mathbf{K}_a \ln\left(\mathbf{V}^e_{a\_\text{inter}}\right) \tag{2}$$

where $J_{a\_\text{inter}} = \det \mathbf{F}^e_{a\_\text{inter}}$ is the elastic intermolecular volume change, $\ln\left(\mathbf{V}^e_{a\_\text{inter}}\right)$ is the Hencky elastic strain and $\mathbf{K}_a$ is the fourth-order elastic stiffness tensor of the isotropic amorphous layers given by:

$$\left[K_{a\_ij}\right]_{6\times 6} = \begin{bmatrix} \lambda+2\mu & \lambda & \lambda & 0 & 0 & 0 \\ \lambda & \lambda+2\mu & \lambda & 0 & 0 & 0 \\ \lambda & \lambda & \lambda+2\mu & 0 & 0 & 0 \\ 0 & 0 & 0 & 2\mu & 0 & 0 \\ 0 & 0 & 0 & 0 & 2\mu & 0 \\ 0 & 0 & 0 & 0 & 0 & 2\mu \end{bmatrix} \tag{3}$$

in which λ and μ are the amorphous Lame's constants.

From the rheological point of view, the molecular network resistance is constituted by a nonlinear spring in series with a viscous dashpot (Fig. 2). The molecular network Cauchy stress $\boldsymbol{\sigma}_{a\_net}$ is given by the Arruda and Boyce (1993) eight-chain model of rubber elasticity introducing the extensibility limit of amorphous chains as a deformation measure:

$$\boldsymbol{\sigma}_{a\_\text{net}} = \frac{1}{J_{a\_\text{net}}} \frac{C_h}{3} \frac{\sqrt{N}}{\lambda^e_{a\_\text{net}}} \mathrm{L}^{-1}\left(\frac{\lambda^e_{a\_\text{net}}}{\sqrt{N}}\right)\left(\mathbf{B}^e_{a\_\text{net}} - \lambda^{e^2}_{a\_\text{net}}\mathbf{I}\right) \tag{4}$$

where two relevant molecular network properties are introduced: the amorphous network hardening modulus $C_h = n_c k\theta$ (in which n_c is the average density of amorphous chains per unit volume, k is the Boltzmann's constant and θ is the absolute temperature) and the average number of molecular units N between entanglements (similar to average length of amorphous chains). The term $\mathbf{I}$ is the identity tensor, $J_{a\_\text{net}} = \det \mathbf{F}^e_{a\_\text{net}}$ is the elastic network

volume change, $\lambda^e_{a\_\text{inter}}$ is the elastic stretch on each chain in the amorphous layers:

$$\lambda^e_{a\_\text{net}} = \left[\frac{1}{3}\text{trace}\left(\mathbf{B}^e_{a\_\text{net}}\right)\right]^{1/2} \tag{5}$$

in which $\mathbf{B}^e_{a\_\text{net}} = J^{-2/3}_{a\_\text{net}}\mathbf{F}^e_{a\_\text{net}}\mathbf{F}^{e^T}_{a\_\text{net}}$ is the isochoric elastic left Cauchy-Green tensor and L^{-1} is the inverse Langevin function $\text{L}(x) = \coth(x) - 1/x$ which can be treated by a Padé approximation: $\text{L}^{-1}(x) \approx x\left(3 - x^2\right)/\left(1 - x^2\right)$.

The time derivative of the deformation gradient tensor writes $\dot{\mathbf{F}}_a = \mathbf{L}_a\mathbf{F}_a$ where $\mathbf{L}_a$ is the gradient tensor of the spatial velocity described by: $\mathbf{L}_a = \mathbf{L}^e_a + \mathbf{L}^{in}_a$ where $\mathbf{L}^e_a = \dot{\mathbf{F}}^e_a\mathbf{F}^{e^{-1}}_a$ is the elastic spatial velocity gradient tensor and $\mathbf{L}^{in}_a = \mathbf{F}^e_a\dot{\mathbf{F}}^{in}_a\mathbf{F}^{in^{-1}}_a\mathbf{F}^{e^{-1}}_a$ is the inelastic spatial velocity gradient tensor. The tensor $\mathbf{L}_a = \mathbf{D}_a + \mathbf{W}_a$ may be further additively decomposed into a symmetric part $\mathbf{D}_a = \left(\mathbf{L}_a + \mathbf{L}^T_a\right)/2$ (stretching rate tensor) and a skew-symmetric part $\mathbf{W}_a = \left(\mathbf{L}_a - \mathbf{L}^T_a\right)/2$ (spin tensor). The Taylor assumption is used such that the deformation gradients in the intermolecular and network resistances are equal: $\mathbf{F}_{a\_\text{inter}} = \mathbf{F}_{a\_\text{net}}$. The cavitation damage associated with progressive nucleation and growth of cavities in the amorphous layers (Zaïri et al., 2011; Mesbah et al., 2021) is neglected and the amorphous inelastic deformation is assumed to be isovolumetric, i.e. $\det\mathbf{F}^{in}_{a\_\text{inter}} = \det\mathbf{F}^{in}_{a\_\text{net}} = 1$. By choosing the inelastic flow irrotational, i.e. $\mathbf{W}^{in}_{a\_\text{inter}} = \mathbf{W}^{in}_{a\_\text{net}} = \mathbf{0}$, the evolution equations of the amorphous inelastic deformation gradients, $\mathbf{F}^{in}_{a\_\text{inter}}$ and $\mathbf{F}^{in}_{a\_\text{net}}$, are given by:

$$\dot{\mathbf{F}}^{in}_{a\_\text{inter}} = \mathbf{F}^{e^{-1}}_{a\_\text{inter}}\mathbf{D}^{in}_{a\_\text{inter}}\mathbf{F}^e_{a\_\text{inter}}\mathbf{F}^{in}_{a\_\text{inter}} \quad \text{and} \quad \dot{\mathbf{F}}^{in}_{a\_\text{net}} = \mathbf{F}^{e^{-1}}_{a\_\text{net}}\mathbf{D}^{in}_{a\_\text{net}}\mathbf{F}^e_{a\_\text{net}}\mathbf{F}^{in}_{a\_\text{net}} \tag{6}$$

The amorphous elastic deformation gradients are then extracted from the multiplicative deformation decomposition: $\mathbf{F}^e_{a\_\text{inter}} = \mathbf{F}_{a\_\text{inter}}\mathbf{F}^{in^{-1}}_{a\_\text{inter}}$ and $\mathbf{F}^e_{a\_\text{net}} = \mathbf{F}_{a\_\text{net}}\mathbf{F}^{in^{-1}}_{a\_\text{net}}$. The amorphous inelastic strain rate tensors, $\mathbf{D}^{in}_{a\_\text{inter}}$ and $\mathbf{D}^{in}_{a\_\text{net}}$, are given by the following flow rules:

$$\mathbf{D}^{in}_{a\_\text{inter}} = \dot{\gamma}_{a\_\text{inter}}\frac{\boldsymbol{\sigma}'_{a\_\text{inter}}}{\sqrt{2}\left\|\boldsymbol{\sigma}_{a\_\text{inter}}\right\|} \quad \text{and} \quad \mathbf{D}^{in}_{a\_\text{net}} = \dot{\gamma}_{a\_\text{net}}\frac{\boldsymbol{\sigma}'_{a\_\text{net}}}{\sqrt{2}\left\|\boldsymbol{\sigma}_{a\_\text{net}}\right\|} \tag{7}$$

where $\left\|\boldsymbol{\sigma}_{a\_\text{inter}}\right\| = \left(\boldsymbol{\sigma}'_{a\_\text{inter}}\boldsymbol{\sigma}'_{a\_\text{inter}}/2\right)^{1/2}$ and $\left\|\boldsymbol{\sigma}_{a\_\text{net}}\right\| = \left(\boldsymbol{\sigma}'_{a\_\text{net}}\boldsymbol{\sigma}'_{a\_\text{net}}/2\right)^{1/2}$ are the effective shear stresses, $\boldsymbol{\sigma}'_{a\_\text{inter}}$ and $\boldsymbol{\sigma}'_{a\_\text{net}}$ are the deviatoric parts and, $\dot{\gamma}_{a\_\text{inter}}$ and $\dot{\gamma}_{a\_\text{net}}$ are the

amorphous intermolecular and network shear strain rates, respectively, given by (Boyce et al., 2000):

$$\dot{\gamma}_{a\_\text{inter}} = \dot{\gamma}_{a,0} \exp\left[-\frac{\Delta G}{k\theta}\left(1 - \frac{\left\|\boldsymbol{\sigma}_{a\_\text{inter}}\right\|}{s}\right)\right] \quad \text{and} \quad \dot{\gamma}_{a\_\text{net}} = C_v \left(\frac{1}{\lambda^{in}_{a\_\text{net}} - 1}\right)\left\|\boldsymbol{\sigma}_{a\_\text{net}}\right\| \tag{8}$$

The left formula of Eq. (8) captures barriers to molecular chain segment rotation in the amorphous layers. The term $\dot{\gamma}_{a,0}$ is the pre-exponential factor, ΔG is the activation energy (which must be overcome for inelasticity begins), s is the shear strength controlling the amorphous chain segment rotation:

$$\dot{s} = \frac{\kappa^n s_0^n}{n} s^{1-n} \dot{\gamma}_{a\_\text{inter}} \tag{9}$$

where s_0 is the initial shear strength, n is the intermolecular hardening coefficient and κ is a factor introduced to take into account the crystal-dependency of concentration of stress transmitters in the amorphous layers.

The right formula of Eq. (8) captures molecular relaxation process in the amorphous layers. The term $\lambda^{in}_{a\_\text{net}}$ must be slightly higher than one at the beginning of the loading process to avoid singularity and ensure stability of the numerical algorithm. It is given by:

$$\lambda^{in}_{a\_\text{net}} = \left[\frac{1}{3}\text{trace}\left(\mathbf{B}^{in}_{a\_\text{net}}\right)\right]^{1/2} + \varsigma \tag{10}$$

in which $\mathbf{B}^{in}_{a\_\text{net}} = \mathbf{F}^{in}_{a\_\text{net}} \mathbf{F}^{in^T}_{a\_\text{net}}$ is the inelastic left Cauchy-Green tensor and ς= 0.01 is the added perturbation coefficient ensuring numerical stability.

The term C_v in Eq. (8) is the amorphous network viscosity coefficient given by:

$$C_v = D\exp\left(-\frac{Q}{R\theta}\right) \tag{11}$$

in which D and Q are two molecular relaxation parameters and R is the universal gas constant.

2.2.2. Elastic-viscoplastic polyethylene crystals

The contribution of the polyethylene crystals may be represented by an elastic spring in series with a viscoplastic dashpot capturing barriers to crystallographic shear in the crystalline phase

(Fig. 2). The crystalline stress tensor $\boldsymbol{\tau}_c$ is constitutively coordinated with the strain as:

$$\boldsymbol{\tau}_c = \mathbf{K}_c : \mathbf{E}_c^e \quad \text{with} \quad \boldsymbol{\tau}_c = J_c \mathbf{F}_c^{e^{-1}} \boldsymbol{\sigma}_c \mathbf{F}_c^{e^{-T}} \tag{12}$$

where $J_c = \det \mathbf{F}_c^e$ is the elastic volume change, $\boldsymbol{\sigma}_c$ is the crystalline Cauchy stress tensor, $\mathbf{E}_c^e = \left(\mathbf{F}_c^{e^T} \mathbf{F}_c^e - \mathbf{I} \right) \Big/ 2$ is the Green-Lagrange strain tensor and $\mathbf{K}_c$ denotes the anisotropic fourth-order elastic stiffness tensor of the orthorhombic crystalline phase of polyethylene taken from the literature (Tashiro et al., 1978):

$$\left[K_{c\_ij} \right]_{6\times 6} = \begin{bmatrix} 7.99 & 3.28 & 1.13 & 0 & 0 & 0 \\ 3.28 & 9.92 & 2.14 & 0 & 0 & 0 \\ 1.13 & 2.14 & 315.92 & 0 & 0 & 0 \\ 0 & 0 & 0 & 3.62 & 0 & 0 \\ 0 & 0 & 0 & 0 & 1.62 & 0 \\ 0 & 0 & 0 & 0 & 0 & 3.19 \end{bmatrix} \text{ [GPa]} \tag{13}$$

The plastic deformation of polyethylene crystals occurs by crystallographic slip that is captured by the following relation to account for the N_s distinct slip systems:

$$\mathbf{L}_c^{in} = \sum_{\alpha=1}^{N_s} \dot{\gamma}_c^{\alpha} \mathbf{R}^{\alpha}, \quad \mathbf{R}^{\alpha} = \frac{1}{2} \left(\boldsymbol{n}^{\alpha} \otimes \boldsymbol{m}^{\alpha} + \boldsymbol{m}^{\alpha} \otimes \boldsymbol{n}^{\alpha} \right) \tag{14}$$

where $\mathbf{R}^{\alpha}$ is the nonsymmetric Schmid tensor with $\boldsymbol{n}^{\alpha}$ and $\boldsymbol{m}^{\alpha}$ are the "slip plane" normal vector and the "slip direction" vector in this plane, respectively, and $\dot{\gamma}_c^{\alpha}$ is the crystalline shear strain rate constitutively coordinated to the resolved shear stress $\tau^{\alpha} = \boldsymbol{\tau}_c : \mathbf{R}^{\alpha}$ via a power law:

$$\dot{\gamma}_c^{\alpha} = \dot{\gamma}_{c,0} \operatorname{sign}\left(\tau^{\alpha} \right) \left| \frac{\tau^{\alpha}}{g^{\alpha}} \right|^{1/m} \tag{15}$$

where $\dot{\gamma}_{c,0}$ is a reference strain rate, m is the strain rate sensitivity parameter and g^{α} is the shear strength of the slip system α listed in Table 1. The term $\operatorname{sign}(x)$ is the signum function defined as:

$$\operatorname{sign}(x) = \begin{cases} -1 & x < 0 \\ 0 & x = 0 \\ 1 & x > 1 \end{cases} \tag{16}$$

The crystalline inelastic deformation gradient $\mathbf{F}_c^{in}$ at time $t_{n+1} = t_n + \Delta t$ is calculated

incrementally using the previous one at time t_n (van Dommelen et al., 2003):

$$\mathbf{F}_c^{in}\left(t_{n+1}\right)=\mathbf{F}_{c\_inc}^{in}\mathbf{F}_c^{in}\left(t_n\right) \tag{17}$$

in which $\mathbf{F}_{c\_inc}^{in}$ is the incremental inelastic deformation gradient for the time increment Δt which can be treated by a Padé approximation:

$$\mathbf{F}_{c\_inc}^{in}\approx\left(\mathbf{I}-\mathbf{L}_c^{in}\Delta t/2\right)^{-1}\left(\mathbf{I}+\mathbf{L}_c^{in}\Delta t/2\right) \tag{18}$$

The crystalline elastic deformation gradient is then extracted from the multiplicative deformation decomposition: $\mathbf{F}_c^e=\mathbf{F}_c\mathbf{F}_c^{in^{-1}}$.

The definition of the mechanical coupling of the crystalline lamella with its corresponding amorphous layer remains unchanged from that initially proposed by Lee et al. (1993a, 1993b) and van Dommelen et al. (2003). Therefore, only a summary of the concept is addressed in the next subsection since the details can be found in the paper abovementioned.

2.3. Volume-averaging

The mechanical coupling between the deformation modes in amorphous and crystalline domains is obtained using as ensemble-volume averaged homogenization procedure a volume-weighted average of the respective phases.

The local Cauchy stress tensor $\boldsymbol{\sigma}_I^i$ of the composite inclusion *i* is given by:

$$\boldsymbol{\sigma}_I^i=f_c^i\boldsymbol{\sigma}_c^i+f_a^i\boldsymbol{\sigma}_a^i \tag{19}$$

in which $\boldsymbol{\sigma}_c^i$ and $\boldsymbol{\sigma}_a^i$ are the local stresses previously defined and, f_c^i and f_a^i are the crystalline and amorphous volume fractions, respectively, expressed as:

$$f_c^i=\frac{f_{c,0}^iJ_c}{f_{a,0}^iJ_a+f_{c,0}^iJ_c}\quad\text{and}\quad f_a^i=\frac{f_{a,0}^iJ_a}{f_{a,0}^iJ_a+f_{c,0}^iJ_c} \tag{20}$$

where $f_{c,0}^i$ and $f_{a,0}^i$ are the corresponding initial volume fractions.

The macroscopic Cauchy stress tensor $\bar{\boldsymbol{\sigma}}$ in the semi-crystalline polymer is obtained by the volume-averaging of the N_I inclusions in the aggregate:

$$\bar{\boldsymbol{\sigma}}=\sum_{i=1}^{N_I}f_I^i\boldsymbol{\sigma}_I^i,\quad f_I^i=\frac{f_{I,0}^iJ_I^i}{\sum_{j=1}^{N_I}f_{I,0}^jJ_I^j}=\frac{1}{N_I} \tag{21}$$

The local inclusion-averaged deformation gradient tensor $\mathbf{F}_I^i$ is given by:

$$\mathbf{F}_I^i = f_{c,0}^i \mathbf{F}_c^i + f_{a,0}^i \mathbf{F}_a^i \tag{22}$$

The latter is equal to the imposed macroscopic deformation of the aggregate of the N_I inclusions, i.e. $\overline{\mathbf{F}} = \mathbf{F}_I^i$. In the latter Taylor assumption, compatibility of deformation is satisfied everywhere by considering the local deformation to be related to the global one in an affine sense. It is obvious that the underlying assumptions to relate local and global responses impact the physical consistency and predictability of the model. A realistic modeling allows to propose a framework avoiding (or at least limiting) the arbitrary inclusion of heuristic parameters. Although the Taylor assumption may be questionable, it has the advantage of being easy to implement compared to more sophisticated micromechanical approaches based on an Eshelby formulation (Mesbah et al., 2021), in particular, regarding the complex coupling existing between microstructure, finite-strain, time-dependency, non-linearity and external mechanical loading. Note that the resulting model, applied here to a broad range of crystallinities, involves a relatively low number of parameters with all a physical meaning. The compatibility condition on the deformation gradients is introduced at the amorphous-crystalline interfaces:

$$\mathbf{F}_c^i \cdot \boldsymbol{x}_0^i = \mathbf{F}_a^i \cdot \boldsymbol{x}_0^i = \mathbf{F}_I^i \cdot \boldsymbol{x}_0^i \tag{23}$$

where $\boldsymbol{x}_0^i$ denotes an arbitrary vector in the plane of the interface spanned by the unit vectors $\boldsymbol{e}_{01}^i$ and $\boldsymbol{e}_{02}^i$ of the local orthogonal basis $\left(\boldsymbol{e}_{01}^i, \boldsymbol{e}_{02}^i, \boldsymbol{e}_{03}^i\right)$ in which $\boldsymbol{n}_0^i = \boldsymbol{e}_{03}^i$ denotes the unit normal vector at the amorphous-crystalline interface in the reference configuration[1]. Additionally, the stress equilibrium condition at the interface between the crystalline lamella

[1] Lamellar surfaces in polyethylene are of the {h0l}-type where the angle between the chain direction and the normal of interface varies between 20° and 40° (Bassett and Hodge, 1981). The initial angle between chain direction and normal of interface is set to be 35°.

and the amorphous layer writes:

$$\boldsymbol{\sigma}_c^i \cdot \boldsymbol{n}^i = \boldsymbol{\sigma}_a^i \cdot \boldsymbol{n}^i = \boldsymbol{\sigma}_I^i \cdot \boldsymbol{n}^i \tag{24}$$

where $\boldsymbol{n}^i$ is the unit normal vector at the amorphous-crystalline interface in the current configuration.

When the crystalline lamella is sheared, the plastic deformation is frozen and the homogeneously plasticized crystals can be then regarded as rigid bodies connecting the amorphous chains and having the possibility to rotate during the stretching of amorphous chains, as conceptually realized in (Guo and Zaïri, 2020) for crystallized rubber systems. The texture evolution is related to the orientation of the amorphous-crystalline interfaces which can be updated at each increment. Considering two independent vectors at time $t=0$, $\delta \boldsymbol{x}_{01}^i$ and $\delta \boldsymbol{x}_{02}^i$, in the crystalline-amorphous interface, they become at time t: $\delta \boldsymbol{x}_1^i = \mathbf{F}^i \delta \boldsymbol{x}_{01}^i$ and $\delta \boldsymbol{x}_2^i = \mathbf{F}^i \delta \boldsymbol{x}_{02}^i$ where $\mathbf{F}^i$ can be either $\mathbf{F}_a^i$, $\mathbf{F}_c^i$ or $\mathbf{F}_I^i$. The normal vector $\boldsymbol{n}^i$ is then obtained by:

$$\boldsymbol{n}^i = \frac{\mathbf{F}^i \delta \boldsymbol{x}_{01}^i \times \mathbf{F}^i \delta \boldsymbol{x}_{02}^i}{\left\| \mathbf{F}^i \delta \boldsymbol{x}_{01}^i \times \mathbf{F}^i \delta \boldsymbol{x}_{02}^i \right\|} = \frac{\mathbf{F}^{i^{-T}} \boldsymbol{n}_0^i}{\left\| \mathbf{F}^{i^{-T}} \boldsymbol{n}_0^i \right\|} \tag{25}$$

with $\mathbf{F}^i \delta \boldsymbol{x}_{01}^i \times \mathbf{F}^i \delta \boldsymbol{x}_{02}^i = \det\left(\mathbf{F}^i\right) \mathbf{F}^{i^{-T}} \boldsymbol{n}_0^i$, the symbol $\times$ meaning the cross product of the vectors.

The model introduces a connection between the polyethylene response, the structure and the physics of the deformation modes of the crystalline and amorphous phases. The combination of amorphous and crystalline stiffness and plastic flow describes the small and moderate-strain response. For the large deformation behavior, two molecular orientation effects that take place as the strain-hardening stage proceeds are taken into account: Amorphous chains network alignment/relaxation and crystallographic orientation. In what follows, the model is applied to the large-plastic deformation of polyethylene materials covering a wide spectrum of the crystallinity.

3. Results and discussion

3.1. Database

3.1.1. Materials

Three commercial polyethylene systems, differing by their molecular topology and molar masses, were ordered from Total Petrochemicals and DOW Chemicals: a Ziegler-Natta high-density ethylene-hexene copolymer (HD) from Total Petrochemicals, a linear low-density ethylene-octene copolymer (LL) and an ultra-low density ethylene-octene copolymer (UL) from DOW Chemicals, both issued from metallocene catalysis. The molecular characteristics of the polyethylene pellets determined by Gel Permeation Chromatography (GPC) are listed in Table 2 (provided by the manufacturers). The high co-unit concentrations for LL and UL interfere with the crystalline lamellae formation, and thus induce lower density and crystal degree than for HD. The crystal morphologies can be observed from the Atomic Force Microscopy (AFM)[2] pictures in Fig. 3. Highly regular stacking of crystal lamellae for HD and wide thickness distributions of both the amorphous layers and the crystal lamellae for LL and UL have been evidenced from Small-Angle X-ray Scattering (SAXS) experiments[3]. The long period $L_p = t_c + t_a$ was extracted from SAXS results and reported in Table 3. The term t_c is the mean crystal lamella thickness and t_a is the mean amorphous layer thickness (see Fig. 1). The long period L_p was computed thanks to the Bragg relation from the scattering vector q obtained by azimuthal integration of the 2D-patterns:

$$L_p = \frac{2n_d\pi}{q} \tag{26}$$

where n_d is the diffraction order.

The lamellae in HD are the longest and thickest ones as observed in Fig. 3. Note that the nearly same long period for LL and UL means distinct t_c values as reported in Table 3. The

[2] AFM images were obtained on 0.5 mm thick films using a Dimension 3100 apparatus from Digital Instruments operated in Tapping Mode. The films were slowly cooled from the melt with free upper surface in order to generate a natural crystallization-induced morphology.

[3] SAXS experiments were carried out on the BM02 beamline of the European Synchrotron Radiation Facility (Grenoble, France) equipped with a 0.1 mm point-focusing collimation and a CCD camera (Princeton Instruments, Trenton NJ, USA) at a distance of 127 cm from the specimen, using a wavelength of 1.54 Å.

latter was estimated as follows:

$$t_c = L_p \frac{\rho}{\rho_c} f_{cw} \tag{27}$$

where ρ is the density of the whole material (Table 2), ρ_c=1.00 g/cm^3 is the density of the crystalline phase and f_{cw} is the crystal weight fraction measured by Differential Scanning Calorimetry (DSC) experiments (Table 3).

The crystal and amorphous volume fractions, f_c and f_a, requested in the constitutive model can be obtained in terms of the thicknesses:

$$f_c = \frac{t_c}{t_c + t_a} \quad \text{and} \quad f_a = 1 - \frac{t_c}{t_c + t_a} \tag{28}$$

Table 3 provides the crystallinity characteristics at room temperature. The specific melting enthalpy ΔH_f was measured by DSC at a scanning rate of 10°C/min under nitrogen flow with a Q100-apparatus from TA Instruments, which has been indium-calibrated. Melting endotherms and the crystallizing exotherms are provided in Fig. 4; The extremums correspond to the melting temperature T_f and the crystallizing temperature T_c. The crystal weight fraction f_{cw} was determined using the following formula:

$$f_{cw} = \frac{\Delta H_f}{\Delta H_{f,0}} \tag{29}$$

in which $\Delta H_{f,0}$ is the melting enthalpy of a theoretically fully crystalline polyethylene (Wunderlich, 1980) taking into account the melting temperature dependence for every crystal concentration (see Table 3).

3.1.2. Large-plastic deformation

The intrinsic large-plastic deformation was obtained using video-controlled tensile mechanical tests. They were performed on an electromechanical Instron-5800 universal testing machine interfaced with a non-contact optical extensometer for the local strains

measurement on dog bone shaped samples[4] of 28 mm gauge length, 8 mm width and 1 mm thickness; The gauge part presents a curvature radius of about 120 mm in order to localize the necking (if any) while minimize the stress triaxiality effect. The local true axial strain rate was controlled to remain strictly constant throughout the tests in the smallest sample cross-section even after necking by regulating the cross-head speed of the testing machine. A series of mechanical tests were carried out to obtain data on the main features of the large-strain plastic deformation at room temperature. Different experiments have been undertaken in the plastic instability:

- Single loading steps up to very large strains for model identification: the sample is stretched to a prescribed strain level of about 1.8 at different constant true strain rates: 0.01 /s, 0.005 /s, 0.001 /s, 0.0005 /s and 0.0001 /s.
- Single loading-unloading steps for model verification: the strain is ramped to a prescribed level at a constant true strain rate of 0.001 /s and then ramped down to zero stress under the same absolute strain rate. Three maximum applied strains are considered: 0.9, 1.2 and 1.5.
- Oligo-cyclic stretching for model verification: The previous sequence is performed repeatedly to determine the progressive stress-softening at maximum applied strain and the accumulation of plastic strain at zero stress with increasing cycle number.

The responses are plotted in the form of true (Cauchy) axial stress[5] versus true (Hencky) axial strain.

3.2. Model identification

The model parameters were identified to fit the constant true strain rate monotonic curves up to very large strains. The values are listed in Tables 4 and 5 for HD, LL and UL. The three polyethylene systems have been represented by an aggregate of 125 two-phase layered composite inclusions. As the local interaction between the two phases reduces the segmental

[4] Although no initial preferential orientation was expected, the samples were cut off in the same direction of 1 mm thick compression-molded sheets; The latter were molded from polyethylene pellets at 180°C for 10 min and slowly cooled to room temperature in order to avoid residual thermal stresses generated during cooling.

[5] The stress was calculated by dividing the value of the force (registered by a standard load cell of 1 kN) with the actual specimen cross-section recorded by the optical extensometer.

mobility of the amorphous chains in the vicinity of the crystalline lamella (see Fig. 1), the mean stiffness of the amorphous layer is expected to be severely modified from a material system to another. Both initial elastic and hardening moduli vary with the crystal content. Besides, the difference in amorphous network properties is consistent to the difference in molar weights (see Table 2) and in chain entanglements that are rejected from crystals to amorphous phase. The higher the crystallinity the more entangled the amorphous phase, showing higher concentration of stress transmitters in the amorphous layers including tie molecules and entanglements (i.e. lesser mean chain length N). The overcoming plastic resistances in the two phases are assumed to be nearly invariant with the crystal content; Only the interaction coefficient changes to consider the morphology effect.

Fig. 5 presents the identification results for the different local true axial strain rates: 0.01 /s, 0.005 /s, 0.001 /s, 0.0005 /s and 0.0001 /s. The solid lines represent the model simulations while the symbols represent the experimental data. The model appears to be relatively effective to capture the influence of the crystallinity on various features of the nonlinear mechanical response along with the nonlinear rate-dependency. Moreover, it is able to reproduce the crystal content effect on the gradual polyethylene response transition from the thermoplastic-like behavior of the HD system to the elastomeric-like behavior of the UL system. However, the low-strain response is captured rather poorly by the model with a divergence that increases with the crystallinity decrease. That can be mainly the result of the elastic properties of the polyethylene crystal taken from the literature and introduced as direct inputs into the model for the three polyethylene systems. Despite the latter, the model adequately reproduces, as the crystal content decreases, the decrease in plastic features (yield strength and strain-hardening ability) along with the decrease in rate-dependency.

3.3. Model results

3.3.1. Microstructure evolution

Highly anisotropic behavior takes place during the strain-hardening stage[6]. In the model, the

[6] From the earlier studies of Peterlin (1975), the prevailing picture of the microstructure evolution due to tensile straining of a semi-crystalline polymer has been stated (Seguela et al., 1998a, 1998b; Bartczak and Kozanecki, 2005; Bartczak and Galeski, 2010; Rozanski and Galeski, 2013); The tensile yielding results from massive

orientation-induced strain-hardening region is governed by both crystallographic orientation and molecular orientation/relaxation of the amorphous phase. The predicted results of the crystallographic texture evolution can be evaluated by means of pole figures. Illustrative examples are presented in Fig. 6 in the un-deformed state and in three precise deformed states for preferential directions. The initially isotropic material with randomly oriented lamellae transforms into an anisotropic material due to the reorientation mechanism of the crystalline lamellae towards the maximum principal stretch direction. The (010) poles spread around the transverse direction (Fig. 6a) while the inclusion interface normals are migrating towards the transverse direction (Fig. 6b). The microstructure evolution can be also analyzed using the local axial stresses and stretches plotted in Figs. 7 and 8, respectively. In the early stage of deformation until yield point, the response is governed by the plastic deformation in the crystalline phase and by the intermolecular interactions in the amorphous phase; Their relative importance depends on the amorphicity. It is worth noticing that the interfacial interactions between crystalline and amorphous domains may form a region in the vicinity of crystalline lamella where the amorphous chain mobility is reduced (see Fig. 1). Due to the loss of chain segmental mobility, the glass transition temperature is expected to be severely modified leading to an enhancement of the intermolecular resistance of the amorphous layers. The latter resistance depends on the crystallinity. For the higher crystalline system, the small-strain tensile yielding, manifested by the initial elastic response followed by the rollover to yield, is predominantly associated with the crystallographic shear in the crystalline phase but also, in a certain extent, with the intermolecular barriers to chain-segment rotation in the minor amorphous phase. In the plastic regime, the extension of chains in the amorphous phase progressively governs the response manifested by the progressive strain-hardening and finally the dramatic strain-hardening at very large strains. For low-crystalline systems, the molecular orientation/relaxation of the amorphous phase dominates the material response in all strain

---

structural modifications accompanied by widely diverse deformation mechanisms in the two constitutive phases. It is determined by the stretching of chains in the amorphous phase occurring in the first place (involving inter-lamellar separation, inter-lamellar shear and lamellar rotation) and by the plastic deformation events in the crystalline lamellae followed by their fragmentation leading to the formation of a fibrillar microstructure at large strains.

range, the contribution of the discrete crystalline lamellae to the overall resistance to deformation being slight and they rather act as junction points in the amorphous matrix.

Non-monotonic conditions being one of the most severe tests for the verification of a constitutive model, its predictive capacities are discussed in the two next subsections using the model parameters previously identified in monotonic loading.

3.3.2. Loading-unloading

The model predictions under a loading-unloading path are depicted in Fig. 9 by comparing them with the experimental observations of the three polyethylene systems. A global view at these plots shows that the unloading path is strain dependent. A good agreement appears between model simulations and experimental data of the HD system. The plastic strain at zero stress is very well predicted by the model. For the LL system, it is satisfactory to observe that the model predicts the nonlinearity of the unloading path when the strain level is large. For more moderate strains, the model is unable to capture the nonlinear unloading path which leads to an overestimation of the plastic strain at zero stress. Indeed, the stiffness evolves during retraction which leads to a strong nonlinear unloading path. The abrupt initial unloading tangent does not allow to the model to reproduce the unloading response of the UL system. The increase in crystal content leads to a gradual transition from a linear unloading response dominated by the stiff crystalline lamellae to a drastic recovery upon unloading dominated by the rubbery amorphous layers. It is satisfactory to observe that the model reproduces, as the crystal content decreases, the decrease in residual strain at zero stress. The latter may be associated to the drastic recovery governed by the network elastic stretch during retraction (Fig. 8).

3.3.3. Oligo-cyclic loading

In order to check further the predictive capabilities of the constitutive model, the cyclic response is presented and discussed. The predicted results are compared to the cyclic experimental data in Fig. 10 for a maximum strain value of 1.5 and ten consecutive cycles. The cyclic response exhibits a Mullins effect common with elastomeric-like materials

characterized by a (i) progressive stress-softening with increasing cycle number, (ii) a hysteresis loop (i.e. a difference between unloading and reloading paths), (iii) an accumulation of plastic strain at zero stress (Drozdov, 2009; Wang et al., 2015; Makki et al., 2017; Guo et al., 2021). Their amounts depend on the amorphous phase fraction. The plastic strain evolution is plotted in Fig. 11 until one hundred consecutive cycles. Note that it is divided by the value at the first cycle. The instantaneous adjustment of the cross-head speed of the testing machine to maintain constant the local strain rate (especially during the necking and post-necking stages if any) induced serrated experimental curves. The observed inflection points on the theoretical evolutions are mainly due to the fact that they are not continuously obtained but are punctually extracted from the cyclic stress-strain curves. The accuracy in the data extraction affects thus the smooth character of the theoretical evolutions. The model ability to capture the plastic strain evolution depends on the amorphous phase fraction. It underestimates the HD and LL data in the first fifty cycles and then overestimates the data, whereas it always underestimates the UL data.

The deformation mechanisms associated to the Mullins effect can be discussed thanks to the plots of Figs. 7 and 8. When the macroscopic strain is retracted to zero macroscopic stress, the local axial stress in the crystalline lamellae is negative in average whereas the local axial stress in the amorphous phase is positive. The further decomposition of the amorphous stress shows a negative intermolecular stress and a positive network stress. Because the previously sheared crystalline lamellae are in a frozen state, the crystalline stress is seen to be stabilized throughout the consecutive deforming cycles. By contrast, the network stress significantly decreases with increasing cycles whereas the intermolecular stress slightly decreases. The inelastic intermolecular stretch is permanent while the inelastic network stretch slightly increases with increasing cycles. In addition to the crystal texturing, a new molecular network configuration appears in the amorphous linking modifying the previous one at each new cycle of the cyclic loading.

It can be observed that prediction and experimental data are close to each other for the HD system but the predicted hysteresis loop diverges from the experimental data with the crystallinity increase. Recall that the elastic properties of the polyethylene crystal are

introduced as direct inputs into the model which leads to the abrupt reloading. Note that the main goal here is to observe the model limitations rather than propose improvements of modeling capabilities. Disregarding the micromechanical scale transition, the simplest way to improve the model capacities could be done by adapting the crystal stiffness for each fraction and/or by introducing a network alteration upon cyclic loading through an appropriate change of the number of entangled points. As some entanglements will become ineffective with increasing cycle number, $C_h = n_c k\theta$ will decrease and N will increase (the product $n_c N$ remaining constant in order to conserve mass) while the other model parameters would remain unchanged. The evolution equations of n_c and N would require supplementary parameters fitted on the hysteretic response evolution with increasing cycle number (Makki et al., 2017). Nonetheless, our objective here is to limit the number of model parameters and to present the model plots for predictive purpose only introducing the crystal content as main variable input.

The quite good agreement with the experimental observations of the HD nonlinear cyclic response confirms the ability of the constitutive representation to describe high crystalline media. Fig. 12 compares the predicted and measured curves to present the strain level effect on different aspects of the HD cyclic response considering both one cycle with increasing maximum strain levels and oligo-cyclic loading with two strain levels. It can be observed that the model recaptures the same path as that corresponding to the monotonic one when the strain exceeds the maximum strain previously applied. The general trends of the oligo-cyclic stretching are adequately predicted by the model, in particular the increase in stress-softening magnitude with strain level.

4. Concluding remarks

In this paper, the highly nonlinear and rate-dependent mechanical response of semi-crystalline polyethylene systems covering a wide spectrum of the crystallinity was investigated within a multi-scale homogenization-based approach. The model ability to capture the large-strain response variation with the crystallinity was criticized. The model exhibited weaknesses in small-strain region but it was able to reproduce, within large-strain region, the rate-dependent

monotonic response variation with crystallinity. The general trends of the high-crystalline material cyclic response were quantitatively well reproduced by the model while the deviation from experiments increased with amorphicity, which would require to take into account the amorphous network alteration.

In addition to molecular orientation effects that takes place as the deformation proceeds, the cavitation damage associated with progressive nucleation and growth of cavities in the amorphous layers will be presented in a future work.

References

Abdul-Hameed, H., Messager, T., Zaïri, F., Naït-Abdelaziz, M., 2014. Large-strain viscoelastic-viscoplastic constitutive modeling of semi-crystalline polymers and model identification by deterministic/evolutionary approach. Computational Materials Science 90, 241-252.

Agoras, M., Ponte Castaneda, P., 2012. Multi-scale homogenization-based modeling of semi-crystalline polymers. Philosophical Magazine 92, 925-958.

Anoukou, K., Zaïri, F., Naït-Abdelaziz, M., Zaoui, A., Qu, Z., Gloaguen, J.M., Lefebvre, J.M., 2014. A micromechanical model taking into account the contribution of α- and γ-crystalline phases in the stiffening of polyamide 6-clay nanocomposites: a closed-formulation including the crystal symmetry. Composites Part B 64, 84-96.

Argon, A.S., Galeski, A., Kazmierczak, T., 2005. Rate mechanisms of plasticity in semicrystalline polyethylene. Polymer 46, 11798-11805.

Arruda, E.M., Boyce, M.C., 1993. A three-dimensional constitutive model for the large stretch behavior of rubber elastic materials. Journal of the Mechanics and Physics of Solids 41, 389-412.

Ayoub, G., Zaïri, F., Naït-Abdelaziz, M., Gloaguen, J.M., 2010. Modelling large deformation behaviour under loading-unloading of semicrystalline polymers: application to a high density polyethylene. International Journal of Plasticity 26, 329-347.

Ayoub, G., Zaïri, F., Fréderix, C., Gloaguen, J.M., Naït-Abdelaziz, M., Seguela, R., Lefebvre, J.M., 2011. Effects of crystal content on the mechanical behaviour of polyethylene under finite strains: experiments and constitutive modelling. International Journal of Plasticity 27, 492-511.

Bartczak, Z., Kozanecki, M., 2005. Influence of molecular parameters on high-strain deformation of polyethylene in the plane-strain compression. Part I. Stress-strain behavior. Polymer 46, 8210-8221.

Bartczak, Z., Galeski, A., 2010. Plasticity of semicrystalline polymers. Macromolecular Symposia 294, 67-90.

Bassett, D.C., Hodge, A.M., 1981. On the morphology of melt-crystallized polyethylene I. Lamellar profiles. Proceedings of the Royal Society of London A 377, 25-37.

Bédoui, F., Diani, J., Régnier, G., Seiler, W., 2006. Micromechanical modelling of isotropic elastic behaviour of semicrystalline polymers. Acta Materialia 54, 1513-1523.

Ben Hadj Hamouda, H., Laiarinandrasana, L., Piques, R., 2007. Viscoplastic behaviour of a medium density polyethylene (MDPE): Constitutive equations based on double nonlinear deformation model. International Journal of Plasticity 23, 1307-1327.

Bernard, C.A., Lame, O., Deplancke, T., Cavaillé, J.Y., Ogawa, K., 2020. From rheological to original three-dimensional mechanical modelling of semi-crystalline polymers: Application to a wide strain rate range and large deformation of Ultra-High Molecular Weight PolyEthylene. Mechanics of Materials 151, 103640.

Boyce, M.C., Socrate, S., Llana, P.G., 2000. Constitutive model for the finite deformation stress-strain behavior of poly(ethylene terephthalate) above the glass transition. Polymer 41, 2183-2201.

Chen, K., Kang, G., Yu, C., Jiang, H., 2019. Effect of crystalline content on ratchetting of ultra-high molecular weight polyethylene polymers: Experimental investigation and constitutive model. Mechanics of Materials 133, 37-54.

Colak, O.U., Dusunceli, N., 2006. Modeling viscoelastic and viscoplastic behavior of high density polyethylene (HDPE). Journal of Engineering Materials and Technology 128, 572-578.

Deplancke, T., Fivel, M., Lame, O., 2019. 1D strain rate-dependent constitutive model of UHMWPE: From crystalline network to fibrillar structure behavior. Mechanics of Materials 137, 103129.

Drozdov, A.D., Gupta, R.K., 2003. Constitutive equations of finite viscoplasticity of semicrystalline polymers. International Journal of Solids and Structures 40, 6217-6243.

Drozdov, A.D., 2009. Mullins' effect in semicrystalline polymers. International Journal of Solids and Structures 46, 3336-3345.

Drozdov, A.D., Klitkou, R., Christiansen, J.D., 2013. Multi-cycle deformation of semicrystalline polymers: Observations and constitutive modeling. Mechanics Research Communications 48, 70-75.

Dusunceli N., Colak, O.U., 2008. Modelling effects of degree of crystallinity on mechanical behavior of semicrystalline polymers. International Journal of Plasticity 24, 1224-1242.

Gueguen, O., Ahzi, S., Makradi, A., Belouetta, S., 2010. A new three-phase model to estimate the effective elastic properties of semi-crystalline polymers: Application to PET. Mechanics of Materials 42, 1-10.

Guo, H., Rinaldi, R.G., Tayakout, S., Broudin, M., Lame, O., 2021. Characterization of the spherulitic deformation in equatorial region and cavitation in HDPE materials submitted to mixed-mode oligo-cyclic tensile loading. Polymer Testing 99, 107208.

Guo, Q., Zaïri, F., 2020. A physically-based thermo-mechanical model for stretch-induced crystallizable rubbers: crystallization thermodynamics and chain-network crystallization anisotropy. International Journal of Plasticity 131, 102724.

Hachour, K., Zaïri, F., Naït-Abdelaziz, M., Gloaguen, J.M., Aberkane, M., Lefebvre J.M., 2014. Experiments and modeling of high-crystalline polyethylene yielding under different stress states. International Journal of Plasticity 54, 1-18.

Haward, R.N., Thackray, G., 1968. The use of a mathematical model to describe isothermal stress-strain curves in glassy thermoplastics. Proceedings of the Royal Society of London 302, 453-472.

Hillmansen, S., Hobeika, S., Haward, R.N., Leevers, P.S., 2000. The effect of strain rate, temperature, and molecular mass on the tensile deformation of polyethylene. Polymer Engineering and Science 40, 481-489.

Kazmierczak, T., Galeski, A., Argon, A.S., 2005. Plastic deformation of polyethylene crystals as a function of crystal thickness and compression rate. Polymer 46, 8926-8936.

Khan, F., Krempl, E., 2006. Amorphous and semicrystalline solid polymers: Experimental and modeling studies of their inelastic deformation behaviors. Journal of Engineering Materials and Technology 128, 64-72.

Lee, B.J., Parks, D.M., Ahzi, S., 1993a. Micromechanical modeling of large plastic deformation and texture evolution in semi-crystalline polymers. Journal of the Mechanics and Physics of Solids 41, 1651-1687.

Lee, B.J., Argon, A.S., Parks, D.M., Ahzi, S., Bartczak, Z., 1993b. Simulation of large strain plastic deformation and texture evolution in high density polyethylene. Polymer 34, 3555-3575.

Makki, M., Ayoub, G., Abdul-Hameed, H., Zaïri, F., Mansoor, B., Naït-Abdelaziz, M., Ouederni, M., Zaïri, F., 2017. Mullins effect in polyethylene and its dependency on crystal content: A network alteration model. Journal of the Mechanical Behavior of Biomedical Materials 75, 442-454.

Mesbah, A., Elmeguenni, M., Yan, Z., Zaïri, F., Ding, N., Gloaguen, J.M., 2021. How stress triaxiality affects cavitation damage in high-density polyethylene: experiments and constitutive modeling. Polymer Testing, 107248.

Mirkhalaf, M., van Dommelen, J.A.W., Govaert, L.E., Furmanski, J., Geers, M.G.D., 2019. Micromechanical modeling of anisotropic behavior of oriented semicrystalline polymers. Journal of Polymer Science, Part B: Polymer Physics 57, 378-391.

Nikolov, S., Doghri, I., 2000. A micro/macro constitutive model for the small-deformation behavior of polyethylene. Polymer 41, 1883-1891.

Nikolov, S., Doghri, I., Pierard, O., Zealouk, L., Goldberg, A., 2002. Multi-scale constitutive modeling of the small deformations of semi-crystalline polymers. Journal of the Mechanics and Physics of Solids 50, 2275-2302.

Peacock, AJ., 2000. Handbook of Polyethylene: Structures, Properties, and Applications. Dekker, M. (Eds.), New York.

Peterlin, A., 1975. Plastic deformation of polymers with fibrous structure. Colloid and Polymer Science 253, 809-823.

Qi, Z., Hu, N., Li, G., Zeng, D., 2019. Constitutive modeling for the elastic-viscoplastic behavior of high density polyethylene under cyclic loading. International Journal of Plasticity 113, 125-144.

Rozanski, A., Galeski, A., 2013. Plastic yielding of semicrystalline polymers affected by amorphous phase. International Journal of Plasticity 41, 14-29.

Seguela, R., Gaucher-Miri, V., Elkoun, S., 1998a. Plastic deformation of polyethylene and ethylene copolymers. Part I Homogeneous crystal slip and molecular mobility. Journal of Materials Science 33, 1273-1279.

Seguela, R., Elkoun, S., Gaucher-Miri, V., 1998b. Plastic deformation of polyethylene and ethylene copolymers. Part II Heterogeneous crystal slip and strain-induced phase change. Journal of Materials Science 33, 1801-1807.

Sepiani, H., Polak, M.A., Penlidis, A., 2018. Modeling short- and long-term time-dependent nonlinear behavior of polyethylene. Mechanics of Advanced Materials and Structures 25, 600-610.

Tashiro, K., Kobayashi, M., Tadokoro, H., 1978. Calculation of three-dimensional elastic constants of polymer crystals. 2. Application to orthorhombic polyethylene and poly(vinyl alcohol). Macromolecules 11, 914-918.

Uchida, M., Tada, N., 2013. Micro-, meso- to macroscopic modeling of deformation behavior of semi-crystalline polymer. International Journal of Plasticity 49, 164-184.

van Dommelen, J.A.W., Parks, D.M., Boyce, M.C., Brekelmans, W.A.M., Baaijens, F.P.T., 2003. Micromechanical modeling of the elasto-viscoplastic behavior of semi-crystalline polymers. Journal of the Mechanics and Physics of Solids 51, 519-541.

Wang, M., Shen, J., Li, J., Guo, S., 2015. Network alteration theory on Mullins effect in semicrystalline polymers. Polymer International 64, 105-112.

Wunderlich, B., 1980. Macromolecular Physics, Crystal Melting, Academic Press, New York.

Zaïri, F., Aour, B., Gloaguen, J.M., Naït-Abdelaziz, M., Lefebvre, J.M., 2006. Numerical modelling of elastic-viscoplastic equal channel angular extrusion process of a polymer. Computational Materials Science 38, 202-216.

Zaïri, F., Naït Abdelaziz, M., Gloaguen, J.M., Lefebvre, J.M., 2011. A physically-based constitutive model for anisotropic damage in rubber-toughened glassy polymers during finite deformation. International Journal of Plasticity 27, 25-51.

Zhang, C., Moore, I.D., 1997. Nonlinear mechanical response of high density polyethylene. Part II: Uniaxial constitutive modeling. Polymer Engineering and Science 37, 413-420.

Table 1. Slip systems and associated shear strength (Lee et al., 1993a).

Slip system	g^{α}(MPa)
(100)[001]	8
(010)[001]	20
{110}[001]	20
(100)[010]	13.3
(010)[100]	20
{110}<1$\bar{1}$0>	17.6

Table 2. Molecular characteristics and density of the three polyethylene systems: number-average molar weight M_n; weight-average molar weight M_w; counit content ξ; density ρ.

Material	M_n (kDa)	M_w (kDa)	ξ (mole%) †	ρ (g/cm^3) *
UL	75	150	12 (60)	0.870
LL	50	104	5.0 (25)	0.902
HD	14	174	0.1 (0.5)	0.959

† hexene for the HD system; octene for the LL and UL systems; between brackets is the short chain branching per 1000 C atoms in the backbone.

* density of compression-molded sheets.

Table 3. Physical characteristics of the three polyethylene systems: long period L_p; mean crystalline thickness t_c; melting enthalpy of a perfect polyethylene crystal $\Delta H_{f,0}$; crystal weight fraction f_{cw}; crystal volume fraction f_c.

Material	L_p (nm)	t_c (nm)	$\Delta H_{f,0}$ (J/g)	f_{cw} (%)	f_c (%)
Experimental method	SAXS	SAXS	DSC	DSC	DSC
UL	13	2	~ 290.3	17.4 ± 0.3	15.1 ± 0.2
LL	14	4.2	~ 299.3	33.3 ± 0.8	30 ± 0.7
HD	26.5	19.2	~ 296.5	75.5 ± 0.8	72.4 ± 0.8

Table 4. HD model parameters.

Crystalline	Reference strain rate	$\dot{\gamma}_{c,0}$	10^{-6} (s^{-1})
	Strain rate sensitivity	m	0.1355
Amorphous	First Lame's constant	λ	100 (GPa)
	Second Lame's constant	μ	200 (MPa)
	Reference strain rate	$\dot{\gamma}_{a,0}$	10^{-6} (s^{-1})
	Activation energy	ΔG	4.03×10^{-20} (J)
	Initial shear strength	s_0	14 (MPa)
	Intermolecular hardening	n	193
	Interaction coefficient	κ	19.6
	Hardening modulus	C_h	1.2 (MPa)
	Chain length	N	26
	Molecular relaxation	D	7.8×10^{28} (MPa^{-1} s^{-1})
	Molecular relaxation	Q/R	25.5×10^{3} (K)

Table 5. UL and LL model parameters (all other parameters are listed in Table 4).

Material	λ (GPa)	μ (MPa)	κ	C_h (MPa)	N
UL	1	2	0.28	0.24	42
LL	16.6	33	1.4	0.8	42

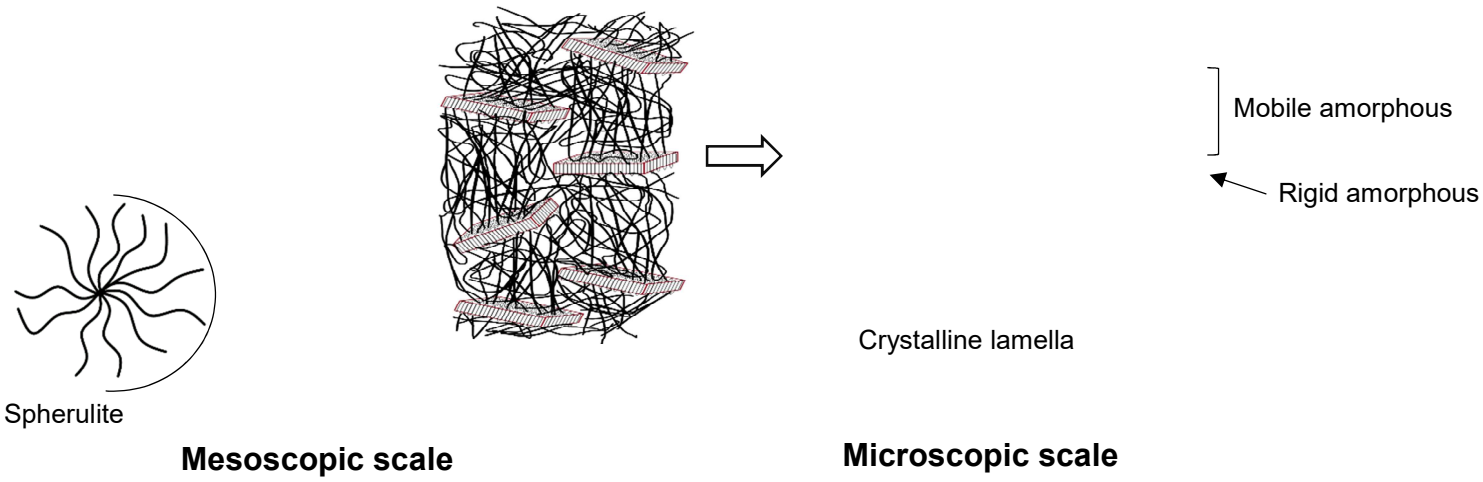

Figure 1. Two-scale view of the semi-crystalline structure; At the mesoscopic scale, the crystalline lamellae may be arranged in highly regular stacking to form spherulitic morphology for high-crystalline media or they may be randomly distributed in the amorphous matrix for low-crystalline media; Both phases are coupled in a complex manner.

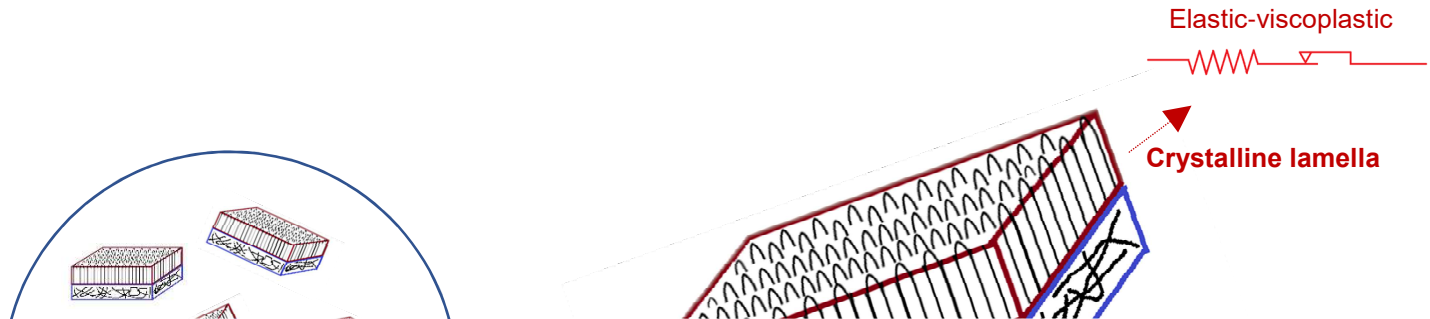

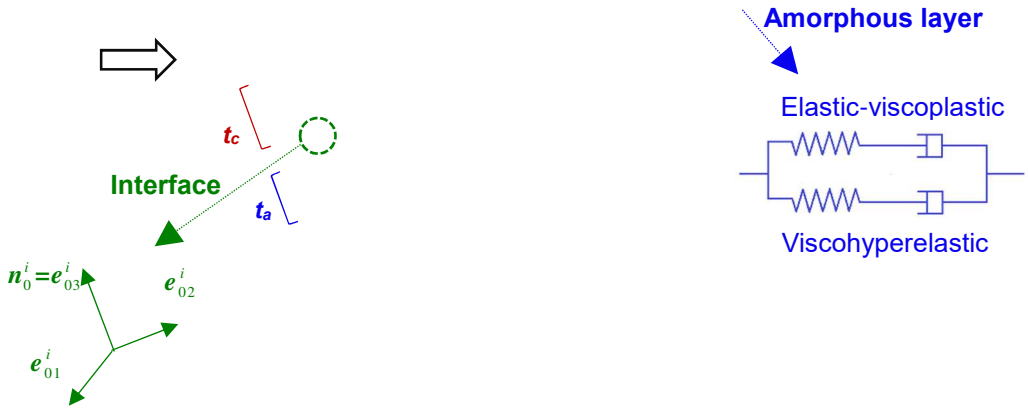

Figure 2. Constitutive representation considering the semi-crystalline medium as an aggregate of randomly distributed two-phase layered composite inclusions. Each inclusion is constituted by a stiff crystalline lamella with an internal elasti-viscoplastic stress and a rubbery amorphous layer with an internal stress including elastic-viscoplastic intermolecular and viscohyperelastic network stresses.

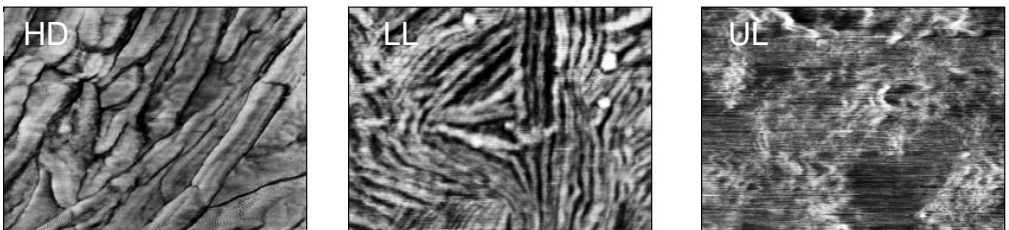

Figure 3. AFM images at different magnifications of the three polyethylene systems showing isotropically distributed stacks of well-defined crystalline lamellae (spherulitic and lamellar morphologies) in the HD and LL systems and fuzzy crystallites akin to fringed micelles (bundle-like crystals embedded in the rubbery amorphous matrix) in the UL system.

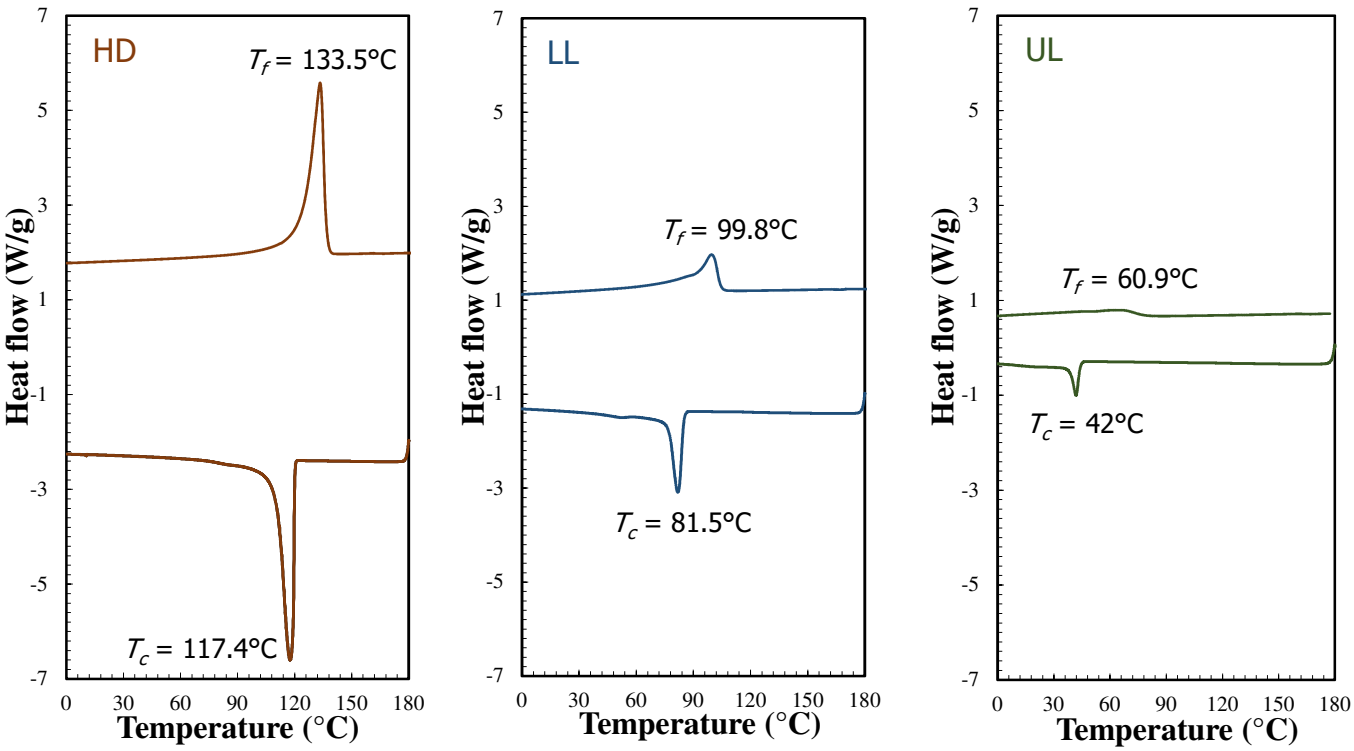

Figure 4. Melting endotherms and cooling exotherms of the three polyethylene systems. The HD heat flow is typical of a high-crystalline polymer. The very broad LL and UL melting endotherms show non-uniform chemical composition distributions due to high co-unit concentrations.

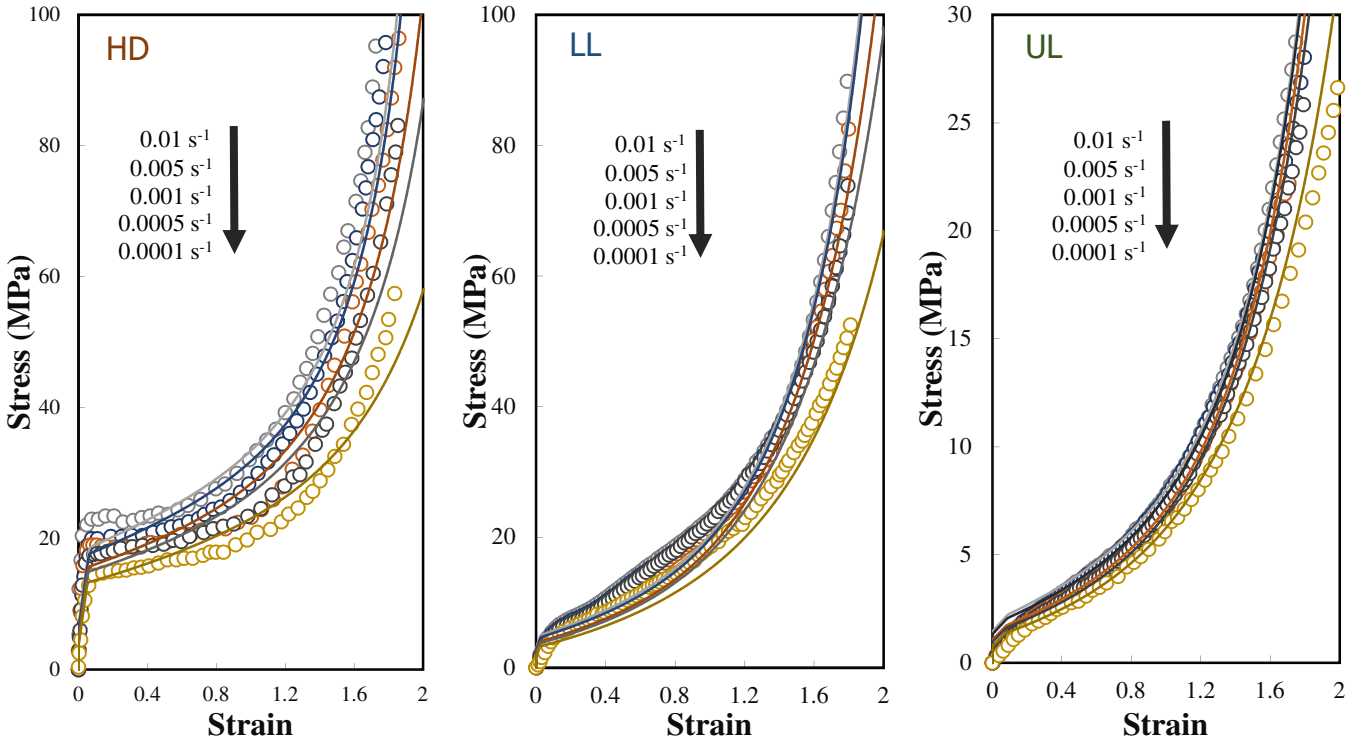

Figure 5. Stress-strain curves of the three polyethylene systems at different true strain rates (symbols: experimental data, solid lines: constitutive model).

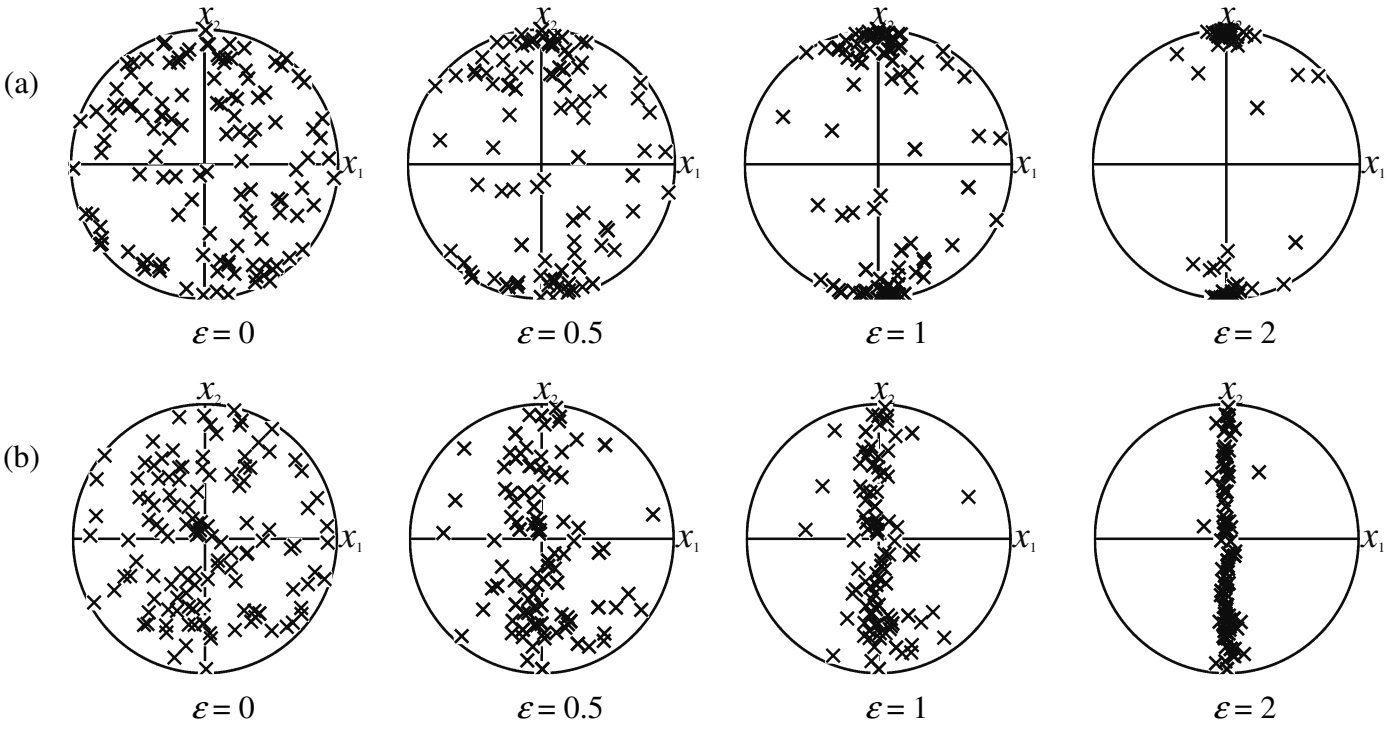

Figure 6. Model predictions of pole figures at different macroscopic strain levels $\varepsilon = \ln(\lambda)$: (a) (010), (b) inclusion normal direction.

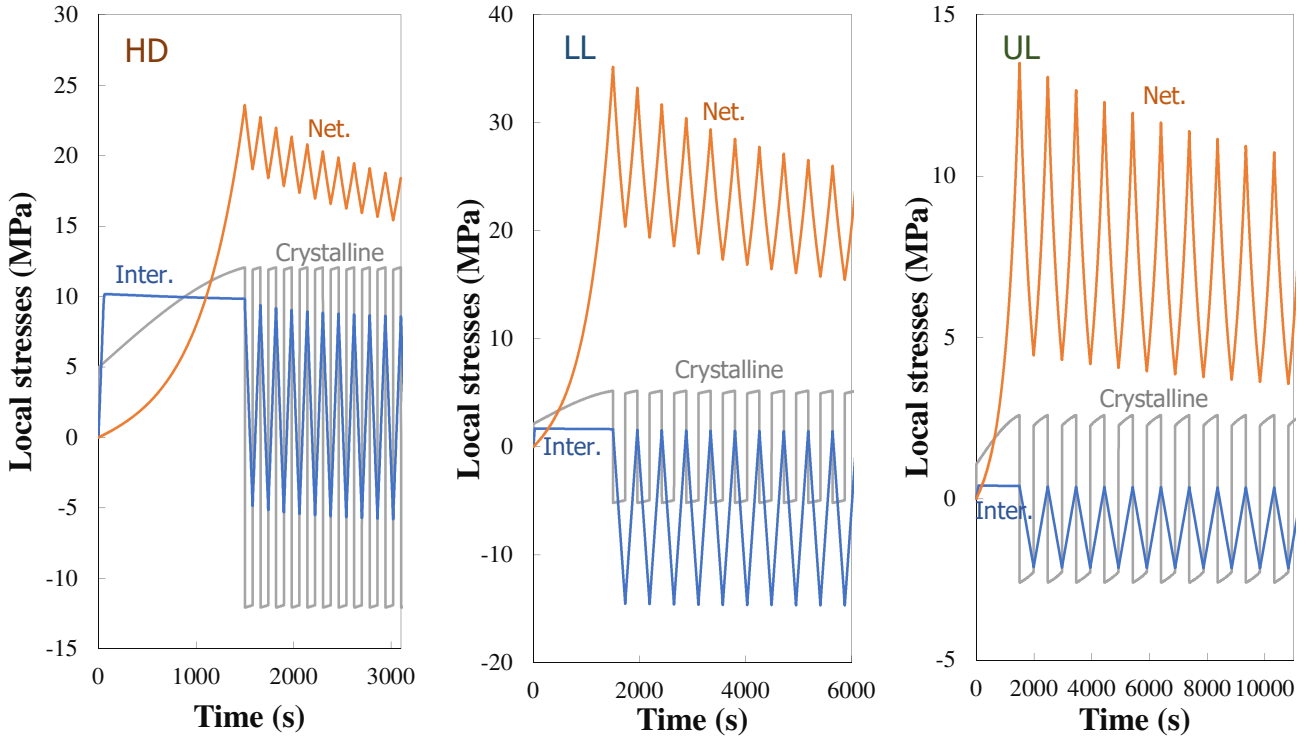

Figure 7. Local axial stresses in the three polyethylene systems upon oligo-cyclic loading at a strain level of 1.5 and at a true strain rate of 0.001 /s.

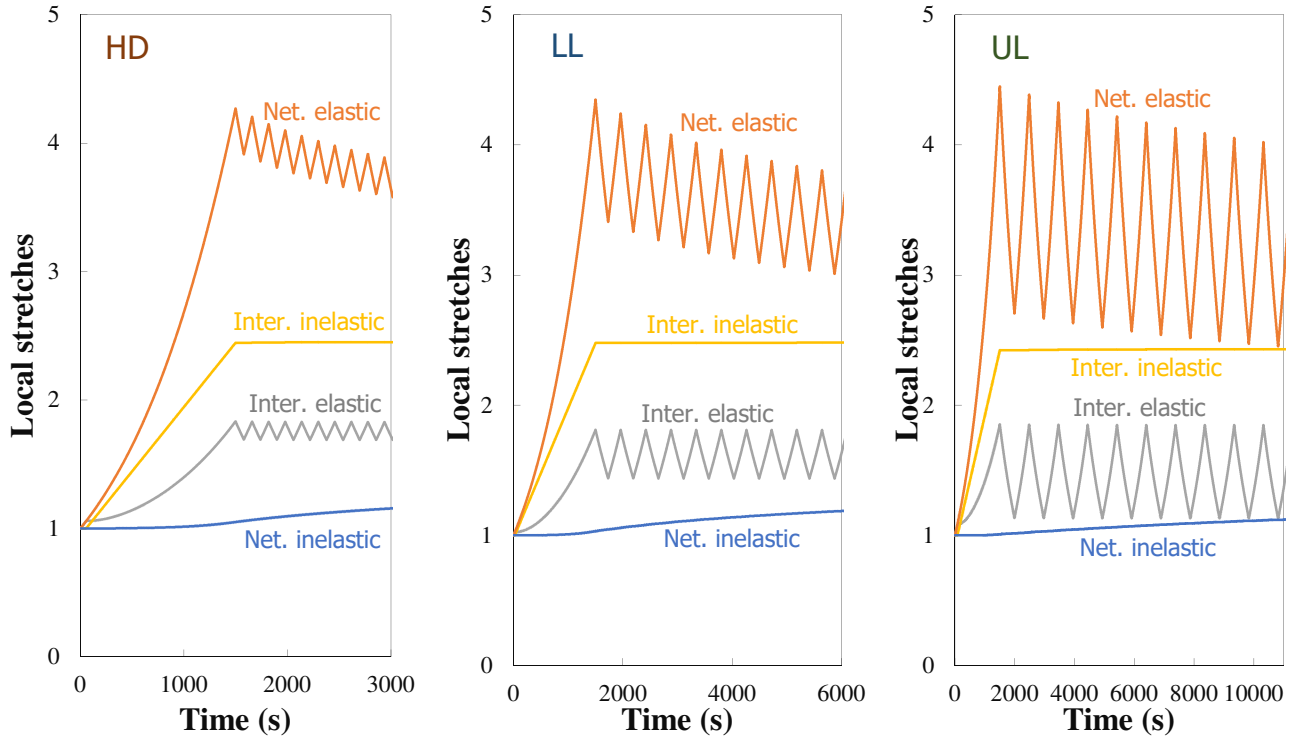

Figure 8. Local axial stretches in the three polyethylene systems upon oligo-cyclic loading at a strain level of 1.5 and at a true strain rate of 0.001 /s.

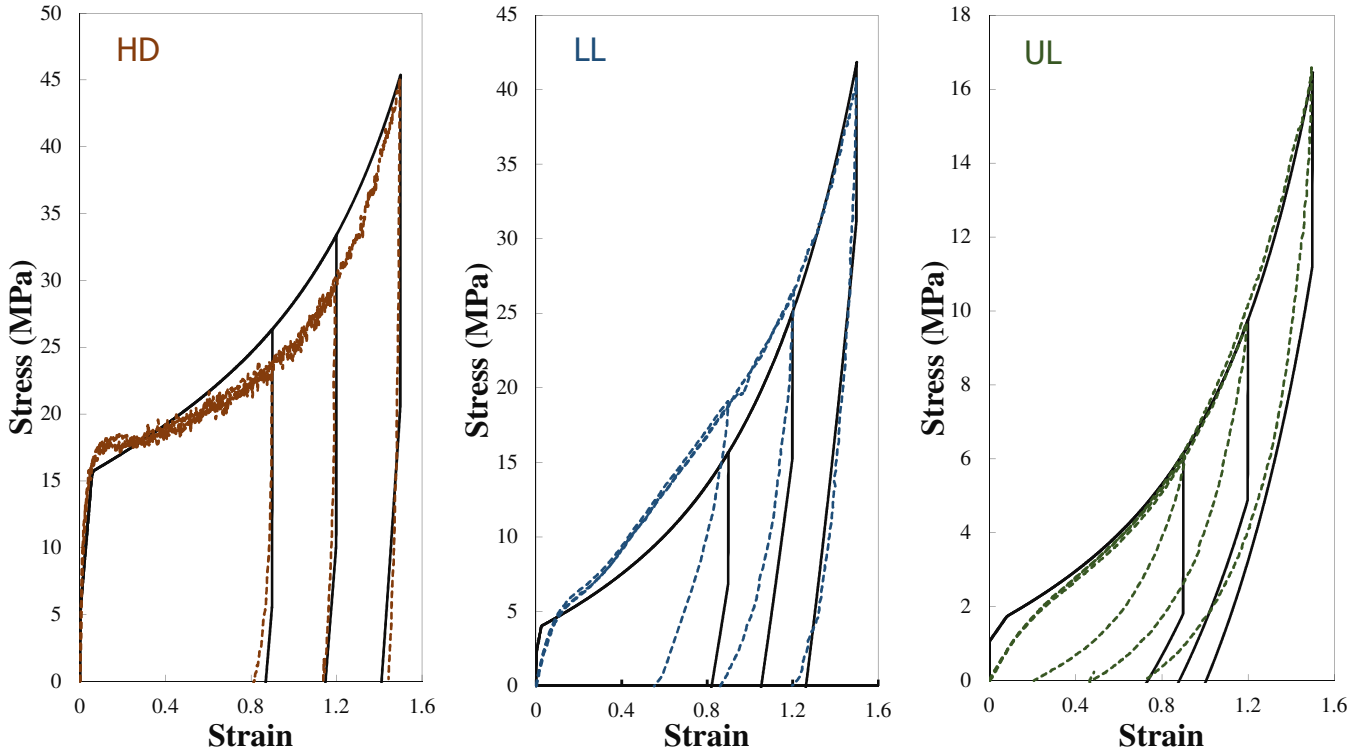

Figure 9. Stress-strain curves of the three polyethylene systems upon loading-unloading at different strain levels and at a true strain rate of 0.001 /s (dashed lines: experimental data, solid lines: constitutive model).

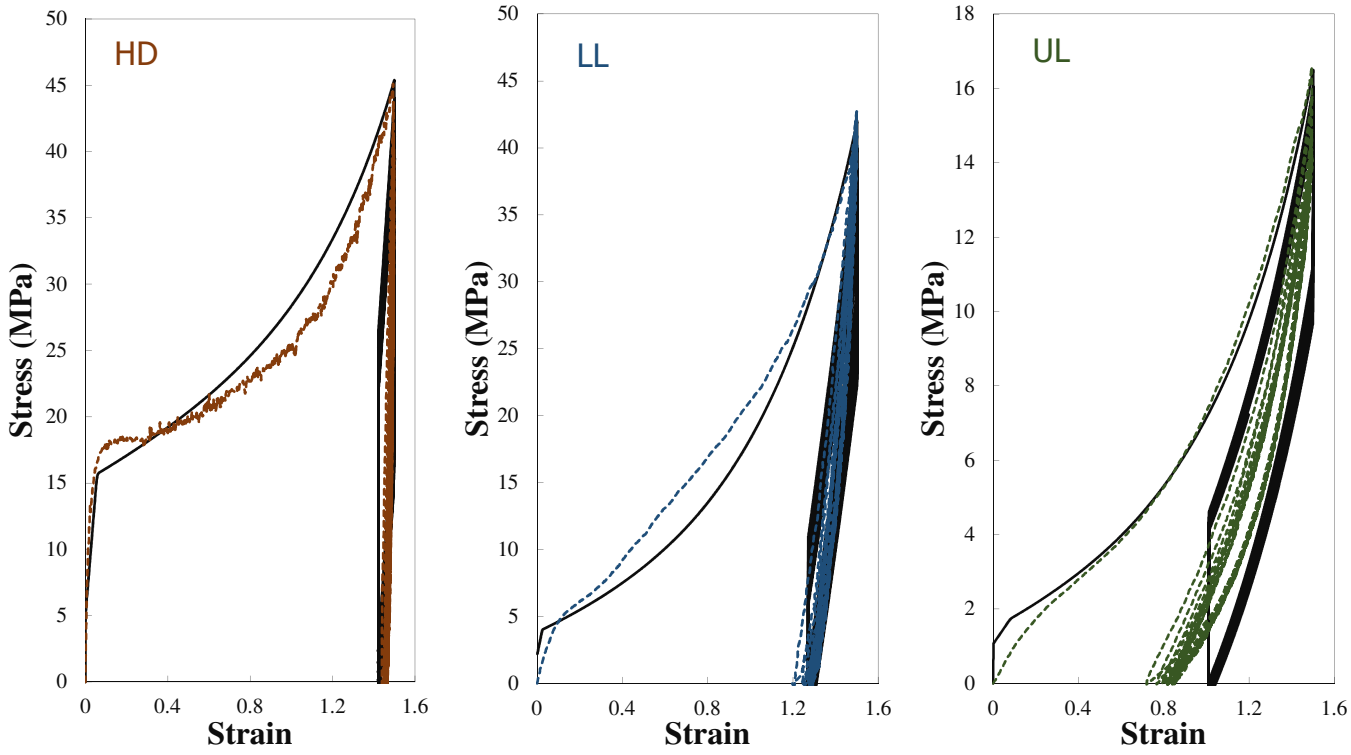

Figure 10. Stress-strain curves of the three polyethylene systems upon oligo-cyclic loading at a strain level of 1.5 and at a true strain rate of 0.001 /s (dashed lines: experimental data, solid lines: constitutive model).

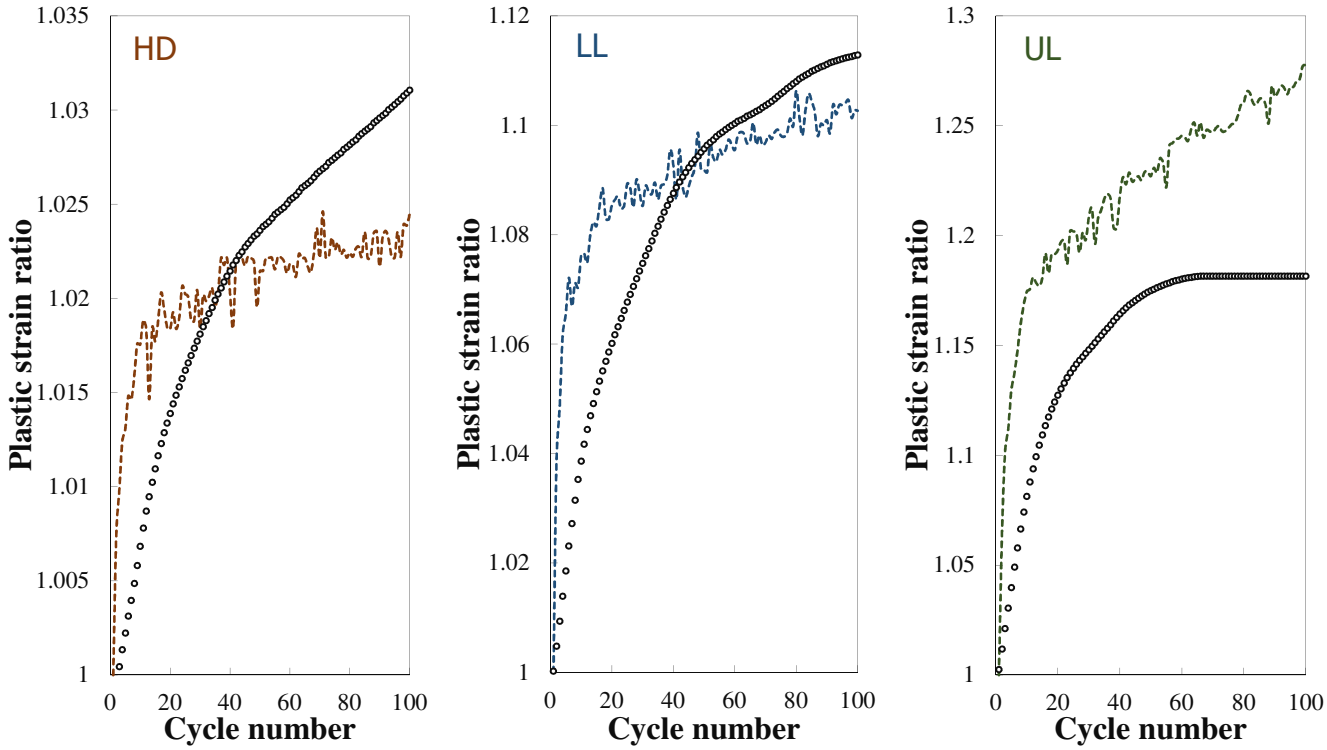

Figure 11. Accumulation of plastic strain at zero stress of the three polyethylene systems upon oligo-cyclic loading at a strain level of 1.5 and at a true strain rate of 0.001 /s (dashed lines: experimental data, symbols: constitutive model).

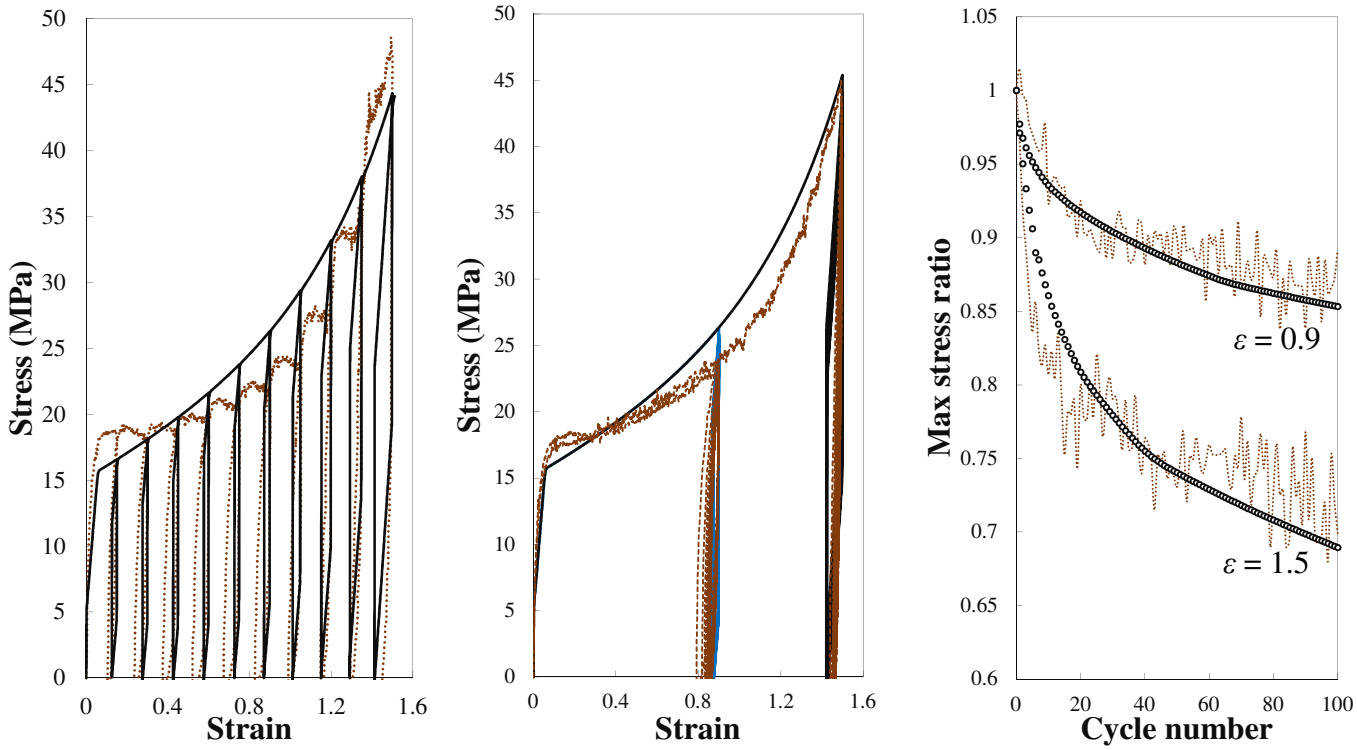

(a) (b) (c)

Figure 12. Stress-strain curves of the HD system upon (a) loading-unloading-reloading, (b) oligo-cyclic loading (dashed lines: experimental data, solid lines: constitutive model), (c) stress-softening at different strain levels and at a true strain rate of 0.001 /s (dashed lines: experimental data, symbols: constitutive model).